Virology 535 (2019) 74–82

Contents lists available at ScienceDirect

Virology

journal homepage: www.elsevier.com/locate/virology

Crystal structure of the S1 subunit N-terminal domain from DcCoV UAE-HKU23 spike protein

Yanwei Cheng[a,b,1], Bin He[a,b,1], Jing Yang[a], Fei Ye[a], Sheng Lin[a], Fanli Yang[a], Zimin Chen[a], Zhujun Chen[a], Yu Cao[a,b,**], Guangwen Lu[a,*]

[a] West China Hospital Emergency Department (WCHED), State Key Laboratory of Biotherapy, West China Hospital, Sichuan University, and Collaborative Innovation Center of Biotherapy, Chengdu, Sichuan, 610041, China
[b] Disaster Medicine Center, Sichuan University, Chengdu, Sichuan, 610041, China

ARTICLE INFO

Keywords:
DcCoV UAE-HKU23
Spike (S)
N-terminal domain (NTD)
Crystal structure
Evolution

ABSTRACT

The DcCoV UAE-HKU23 coronavirus is a newly-found betacoronavirus (betaCoV) that can infect human cells. The viral spike protein plays pivotal roles in mediating receptor-recognition and membrane-fusion, and is therefore a key factor involved in viral pathogenesis and inter-species transmission. Here we reported the structural and functional characterization of the spike N-terminal domain (NTD) from DcCoV UAE-HKU23 (HKU23-NTD). Via mucin-binding assays, we showed that HKU23-NTD is able to bind sugars. We further solved the structure of HKU23-NTD, performed structure-guided mutagenesis and successfully located the potential sugar-binding pockets in the structure. Furthermore, via comparison of available betaCoV NTD structures, we demonstrated that betaCoV NTDs contain a conserved β-sandwich core, but exhibit variant folds in the peripheral elements located in the top-ceiling region and on the lateral side. While showing different compositions and structures, these peripheral elements are topologically equivalent β-sandwich-core insertions, highlighting a divergent evolution process for betaCoVs to form different lineages.

1. Introduction

Coronaviruses (CoVs), within the family of *Coronaviridae* in the *Nidovirales* order, are enveloped, positive-sense, single-stranded RNA viruses. These viruses can be further classified into four genera: Alpha-, Beta-, Gamma-, and Deltacoronavirus (de Groot et al., 2013). CoVs exhibit a propensity for interspecies transmission and pose a severe threat to the global public health, leading to enormous socioeconomic disruptions each year. Currently, six known CoVs can infect humans, including the alphaCoVs hCoV-NL63 and hCoV-229E and the betaCoVs HCoV-OC43, HKU1, severe acute respiratory syndrome (SARS)-CoV and Middle East respiratory syndrome (MERS)-CoV (Bermingham et al., 2012; Li et al., 2007; Vabret et al., 2003; Wang et al., 2014b; Weinstein, 2004; Woo et al., 2005). As the notorious examples of CoVs crossing species barriers, SARS-CoV and MERS-CoV, are both zoonotic pathogens originating from animals. Studies have shown that the two viruses have experienced similar cross-species transmission routes such that they "jumped" from their natural hosts first to an intermediate adaptive animal and then to humans (Lu et al., 2015). Such interspecies transmission events are largely unpredictable and therefore could have severe public health consequences. In 2002–2003, SARS-CoV first emerged in China and swiftly spread to other parts of the world, leading to more than 8000 infection cases with a fatality rate of ~10% (Weinstein, 2004). A decade later, MERS-CoV was discovered in the Middle East and has thus far spread to over 27 countries, causing a total of 2298 laboratory-confirmed infections and 811 associated deaths as of 30th January 2019 (WHO, 2019). These continuously occurring yet unpredictable events of betaCoVs repeatedly crossing species barriers have caused special attention to focusing on betaCoVs. Dissecting the interspecies transmission potentials for other, especially the newfound, members of the genus has become an active area of CoV research.

Phylogenetically, betaCoVs can be categorized into four (A, B, C and D) evolutionary lineages. The human infective betaCoVs of HCoV-OC43 and HKU1 are grouped into lineage A, while SARS-CoV and MERS-CoV belong to lineages B and C, respectively (Forni et al., 2017; Su et al., 2016). In 2013, a novel member of lineage A betaCoVs, the dromedary

* Corresponding author.
** Corresponding author. West China Hospital Emergency Department (WCHED), State Key Laboratory of Biotherapy, West China Hospital, Sichuan University, and Collaborative Innovation Center of Biotherapy, Chengdu, Sichuan, 610041, China.
E-mail addresses: caoyu@wchscu.cn (Y. Cao), lugw@scu.edu.cn (G. Lu).
[1] These authors contributed equally to this work.

https://doi.org/10.1016/j.virol.2019.06.015
Received 21 February 2019; Received in revised form 18 June 2019; Accepted 26 June 2019
Available online 27 June 2019
0042-6822/

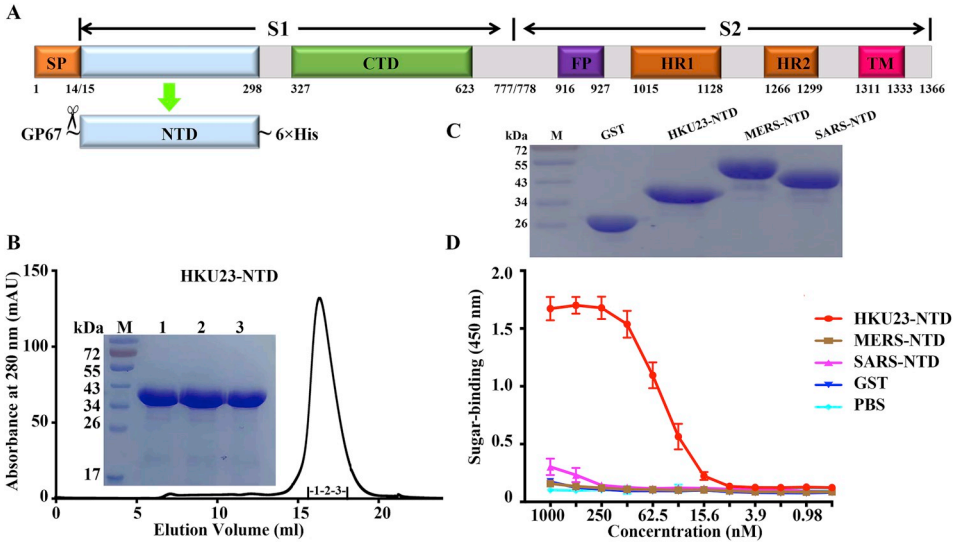

Fig. 1. Biochemical characterization of the purifiedHKU23-NTD protein. (A) A schematic view of the HKU23 spike protein. The indicated domains and elements (SP, signal peptide; NTD, N-terminal domain; CTD, C-terminal domain; FP, Fusion peptide; HR, Heptad repeat; TM, transmembrane domain) are marked with the boundary residue numbers. For HKU23-NTD preparation, the NTD region spanning residues 15–298 was engineered to include an N-terminal GP67 signal peptide and a C-terminal 6 × His tag before expression in insect cells. (B) Purification of the HKU23-NTD protein by size exclusion chromatography. The separation chromatograph of the protein on a calibrated superdex 200 increase column and the SDS-PAGE analyses of the pooled samples were shown. (C) SDS-PAGE analyses of the indicated proteins used for sugar-binding experiments. (D) A mucin-based ELISA assay characterizing the interactions of the indicated proteins (two-fold serial dilutions, starting at 1 μM) with sugars. Both PBS and the GST protein were used as the irrelevant control samples.

camel coronavirus UAE-HKU23 (DcCoV UAE-HKU23), was initially identified through genomic sequencing in fecal samples from dromedaries in Dubai, United Arab Emirates (Woo et al., 2014). Subsequently, the live DcCoV UAE-HKU23 virus was successfully isolated from the human-derived cell line of HRT-18G (human rectal tumor epithelial) cells (Woo et al., 2016), suggesting that DcCoV UAE-HKU23 has evolved to recognize unknown human receptor/(s) and gained the capacity to infect human cells. It is well known that MERS-CoV is probably originated in bats and transmitted to humans using dromedaries as an intermediate host (Al-Tawfiq and Memish, 2014). In light of the fact that dromedaries can host both DcCoV UAE-HKU23 and MERS-CoV and that DcCoV UAE-HKU23 is able to infect human cells, it has raised the alert over a potential pandemic caused by the DcCoV UAE-HKU23 virus or its variants. In such a context, knowledge on the virus relevant to its interspecies-transmission potentials would be of vital importance in understanding the viral pathogenesis and in providing new opportunities for human intervention in potential infection cases.

Receptor recognition is a key factor determining the tissue tropism, host specificity, and interspecies-transmission of a virus. In CoVs, this process is mediated by the envelope-interspersed surface-located trimeric spike (S) glycoprotein (Gallagher and Buchmeier, 2001). In most cases of virus entry, coronaviral S needs to be further cleaved by host proteases into a S1 subunit which is responsible for receptor binding and a S2 subunit that functions to mediate membrane fusion (Lai et al., 2007). S1 sequences diverge across different genera but are relatively conserved within each genus. S1 contains two independent domains, an N-terminal domain (NTD) and a C-terminal domain (CTD), either or both of which can function as a receptor-binding entity. For instance, the CTD of SARS-CoV, a typical lineage B betaCoV member, could recognize a proteinaceous receptor, angiotensin-converting enzyme 2 (ACE2) (Li et al., 2003). MERS-CoV and HKU4, both belonging to lineage C, use their CTDs to engage dipeptidyl peptidase 4 (DPP4, also called CD26) for receptor binding (Lu et al., 2013; Wang et al., 2014a). In lineage A, mouse hepatitis coronavirus (MHV) uses its NTD to recognize the proteinaceous receptor of carcinoembryonic antigen-related cell adhesion molecule 1 (CEACAM1), whereas bovine coronavirus (BCoV) and HCoV-OC43 utilize their NTDs to interact with the sugar moiety of 5-N-acetyl-9-O-acetylneuraminic acid (Neu5,9Ac2) to facilitate virus entry (Peng et al., 2011, 2012). It is notable that the sugar-binding capacity of a CoV seems relevant to the presence or absence of a functional hemagglutinin esterase (HE) protein which harbors the receptor-destroying enzyme (RDE) activity. Both HCoV-OC43 and BCoV encode a functional HE which is believed to destroy the sugar receptors late in the infection cycle, thereby enabling viral detachment from sugars on infected and/or nonpermissive host cells (Desforges et al., 2013; Zeng et al., 2008). For most CoVs, however, they do not encode functional HEs and have evolved to either reserve very-weak sugar-binding capacity (such as in MERS-CoV (Li et al., 2017)) or completely lose its sugar-binding activity (such as in MHV (Peng et al., 2011)) in their spikes. An HE gene was identified in the genome of DcCoV UAE-HKU23 (Woo et al., 2014). In addition, the spike NTD of DcCoV UAE-HKU23 (HKU23-NTD) shows a high sequence identity to that of BCoV, a prototypic sugar-binding CoV. These bioinformatic analyses are highly indicative of a similar sugar-engagement capability for the DcCoV UAE-HKU23 virus. However, any functional and structural characterization on HKU23-NTD has been lacking thus far.

In this study, we first prepared high-purity HKU23-NTD protein from insect cells via the Bac-to-Bac Baculovirus Expression System. The sugar-engagement capacity of the protein was then demonstrated via the mucin-binding assay. Furthermore, we successfully determined the atomic structure of HKU23-NTD by x-ray crystallography. Via the structure-guided mutagenesis, the basis of the protein interacting with sugars was delineated. Finally, through a detailed comparison of the available betaCoV NTD structures, we provided structural insights into the evolution of the betaCoV NTD proteins.

2. Results

2.1. Sugar-binding capacity of HKU23-NTD

The full-length S protein of DcCoV UAE-HKU23 (362F strain) is composed of 1366 amino acids. Bioinformatic characterization of the protein sequence has revealed at the protein N-terminus a signal peptide (SP), within the S1 subunit an NTD and a CTD, and within the S2 subunit a predicted fusion peptide (FP), two hydrophobic residue-rich heptad repeat motifs (HR1 and HR2), and a transmembrane domain (TM) (Fig. 1A). While increasing evidence showed that the S protein NTD is the authentic sugar-binding entity in CoVs (Hulswit et al., 2019; Kunkel and Herrler, 1993; Peng et al., 2011, 2012; Schultze et al., 1991), we therefore set out to determine if HKU23-NTD is able to interact with sugars to facilitate virus entry.

Following previous studies reporting recombinant expression of CoV NTDs in insect cells (Yuan et al., 2017), we similarly prepared HKU23-NTD from insect cells via the Bac-to-Bac Baculovirus Expression System.

A GP67 signal peptide (Lu et al., 2013) was engineered to the HKU23-NTD N-terminus to guarantee effective secretion of the protein, and a C-terminal 6× His tag was added to facilitate purification (Fig. 1A). Subsequently, the protein was first harvested from the insect cell culture medium via affinity chromatography and then purified to homogeneity via gel filtration. Its well-behavior of being eluted as a symmetric peak on a gel filtration column revealed good biochemical characteristics of the purified protein. The SDS-PAGE analyses further demonstrated its high purity (Fig. 1B).

A mucin based ELISA assay was then conducted to test if HKU23-NTD could react with sugars. Mucin, a mixture of highly glycosylated proteins containing abundant sugar moieties, has been shown to provide a good substrate for analysis of the sugar binding properties of CoV S proteins (Hulswit et al., 2019; Peng et al., 2011, 2012; Ravindranath et al., 1985). To this end, the GST protein (used as an irrelevant protein control) and NTD proteins from SARS-CoV and MERS-CoV (SARS-NTD and MERS-NTD) were included in the assay in parallel with HKU23-NTD (Fig. 1C). As expected, GST did not bind to mucin. In addition, neither SARS-NTD nor MERS-NTD interacted with mucin which falls in good accordance with previous reports (Li et al., 2017; Peng et al., 2011). In such a context, intimate and concentration-dependent interactions with the bovine submaxillary gland mucin (BSM) was observed for HKU23-NTD (Fig. 1D). The result therefore provided solid evidence that HKU23-NTD possesses the sugar-binding capability, suggesting sugars may be an attachment receptor determinant for DcCoV UAE-HKU23 virus infection.

2.2. Atomic structure of HKU23-NTD

We further set out to investigate the structural features of HKU23-NTD via crystallography. The protein was successfully crystallized in space group C2, and the structure was eventually determined at the resolution of 2.5 angstrom (Å) (Table 1) by molecular replacement using the structure of the NTD protein from BCoV (BCoV-NTD) (PDB code: 4H14) as the search model. High-quality electron density map enables us to unambiguously model the whole polypeptide chain of HKU23-NTD extending from V15 to K298. These amino acids fold into a compact structure, which can be further divided into a large β-sandwich core and several peripheral structural elements (Fig. 2).

Table 1
Data collection and refinement statistics.

	HKU23-NTD
Data collection	
Space group	C2
Cell dimensions	
a, *b*, *c* (Å)	123.59, 46.88, 75.73
α, β, γ (°)	90, 122, 90
Wavelength (Å)	0.97853
Resolution (Å)[a]	32.61–2.50 (2.59–2.50)
Rsym	0.118 (0.299)
R_{mean}	0.132 (0.335)
$R_{p.i.m.}$	0.058 (0.147)
I/σI	14.826 (4.657)
Completeness (%)	99.1 (96.9)
Redundancy	4.9 (4.7)
Refinement	
Resolution (Å)	32.61–2.50
Rwork/Rfree	0.2009/0.2557
No. of atoms	
Protein	2335
Ligand/ion	0
Water	51
B-factors	
Protein	40.2
Ligand/ion	0
Water	36.4
r.m.s.d.	
Bond lengths (Å)	0.007
Bond angles (°)	1.156
Ramachandran plot	
Ramachandran favored (%)	96.1
Ramachandran allowed (%)	3.9
Ramachandran outliers (%)	0

Highest resolution shell statistics are shown in parentheses.

The core sandwich comprises in total sixteen anti-parallel β-strands, assembling into three (upper, middle, and lower) β-sheet layers (Fig. 2). The upper and the middle layers, with relative flat sheet surface, consist of six (β4, β6 - β9 and β13) and seven (β1, β3, β5 and β10 - β12, and β14) strands, respectively. They are stacked together through extended hydrophobic interactions, forming a structural entity whose topological arrangement mode shows a substantial homology to that of human galectin-3 (galactose-binding lectin). A disulfide linkage (C160 to C193) is observed in this region, locking strand β8 with β9. The lower layer is composed of three (β2, and β15, β16) β-stands, two (β2 and β15) of which are of bent conformation. This has led to an apparent curved sheet-surface in the layer. Overall, the three layers are arranged in a parallel manner, forming a sandwich-like structure that accounts for ~62% of the total molecular mass of the NTD protein.

Surrounding the sandwich core, the peripheral structural elements include a top ceiling-like structure, a lateral β-hairpin, and a bottom α-helix (Fig. 2). The ceiling structure, which covers the top surface of the β-sandwich, contains six (β1′- β3′ and β6′ - β8′) small β-strands and two helices (α1 and α2) but is mainly constituted by long loops. In light of the intrinsic flexibility commonly observed in loops, this ceiling structure is, to a large extent, stabilized by two disulfide bonds individually formed by the C21/C156 and C172/C252 pairs. The lateral β-hairpin is composed of strands β4′ and β5′ as well as their connecting loop. It is topologically an element insertion between the upper-layer strand β6 and the middle-layer strand β5 and sterically locating at the lateral side of the sandwich core. Finally, a single helix (α3) was observed to reside underneath the β-sandwich lower layer. A fourth disulfide bond (C286 to C296) links the helix to the sandwich core, thereby stabilizing its conformation.

Throughout the structure, we also clearly observed three N-glycan decorated Asparagine (Asn, N) residues, all of which are located in the β-sandwich region. These include two (N133 and N198) in the upper β-layer and one (N59) in the lower layer (Fig. 2).

2.3. Conserved sugar binding pocket/(s) in HKU23-NTD

In order to gain insight into the molecular basis of the interactions between HKU23-NTD and sugars, we further scrutinized our structure to characterize its potential sugar-binding pocket/(s). Previous mutagenesis studies in BCoV-NTD have revealed a critical sugar-engagement tetra-residue motif (TRM) composed of Y162, E182, W184 and H185(Peng et al., 2012). These four amino acids belong to the top ceiling region, sterically locating in the disulfide-locked ceiling element constituted by two β-strands (β6′ and β7′) and one helix (α2), as well as their flanking loops. This ceiling element bent over the upper β-layer of the sandwich core to form, together with the upper layer strands β7 - β9, an extended pocket (designated as pocket A) where sugars are proposed to bind (Fig. 3A). In addition, a second sugar-binding pocket (denoted pocket B) was recently identified in the top ceiling region of porcine hemagglutinating encephalomyelitis virus (PHEV)-NTD (PDB code: 6QFY) (Hulswit et al., 2019) and HCoV-OC43-NTD (PDB code: 6OHW) (Alejandra Tortorici et al., 2019). Key sugar engagement residues in the pocket, including K81, T/S83 and W90, reside in the inter-strand β3/β4 element. Two small β-strands (β2′ and β3′) and one helix (α1) are observed to form in the element. They are further lined on one side by an N-terminal element, forming a pocket of smaller size (Fig. 3B and C). Sterically, pockets A and B are in proximity to each other. In addition, the N-terminal element of pocket B is further linked to the disulfide-locked ceiling element of pocket A via a disulfide bond (Fig. 3A–C).

In comparison to the NTDs of BCoV, PHEV and HCoV-OC43,

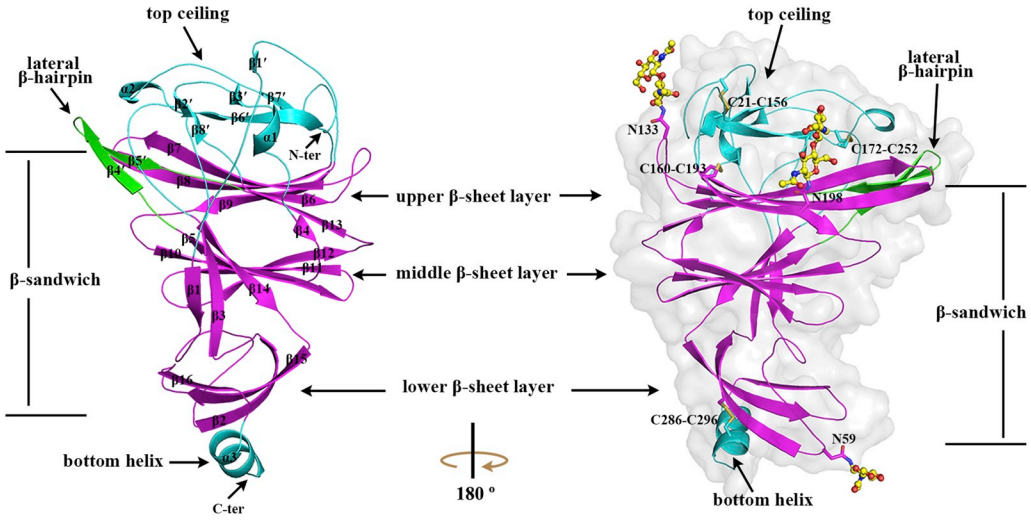

Fig. 2. Overall structure of the HKU23-NTD protein. The β-sandwich core is divided into the upper, middle and lower β-sheet layers, which are colored magenta and labeled. The peripheral elements contain a top ceiling-like structure, a lateral β-hairpin, and a bottom α-helix, which are colored cyan, green, and cyan, respectively. The N- and C-terminus are marked. The glycan-moieties and the disulfide bonds are displayed in sticks and marked in the right panel, which is generated by rotation of the left panel for ~180° around a vertical axis.

HKU23-NTD shows an essentially the same structure with root mean square deviations (r.m.s.d) ranging from 0.71 Å to 0.88 Å over equivalent Cα atoms (Table 2). Accordingly, HKU23-NTD folds to build two quite resembled pockets and contains conserved critical residues with similar conformations and steric positions within the pockets (Fig. 3D). To verify the key functions of these amino acids in the sugar engagement by HKU23-NTD, residues E182, W184, H185 in pocket A and K81, T83, W90 in pocket B are mutated either individually or in combination. We then performed the mucin-binding assay using these mutant proteins by ELISA. As expected, residue substitutions in both pockets dramatically jeopardized the sugar binding capacity of the protein. While single mutants of $E^{182}A$, $W^{184}A$ and $H^{185}A$ in pocket A showed significantly decreased sugar binding, the substitutions in pocket B ($W^{90}A$, $K^{81}A+T^{83}A$ double mutant, as well as the triple mutant) all led to a complete loss in sugar recognition (Fig. 3I).

It is notable that equivalent pockets could also be observed in other available structures of the betaCoV NTDs (including the NTDs of MHV (Peng et al., 2011) and HKU1 (Kirchdoerfer et al., 2016) (MHV-NTD and HKU1-NTD), SARS-NTD, and MERS-NTD (Yuan et al., 2017)). MHV- and HKU1-NTD, however, possess a pocket A of smaller size due to the shortened upper-layer strands and exhibit variant conformations for the equivalent residues within pocket B (Fig. 3E–F). For SARS- and MERS-NTD, owing to variant ceiling-element structures, both pockets are of quite different compositions and conformations from those in HKU23-NTD (Fig. 3G–H). Accordingly, no or only marginal sugar-binding activities are reported for these viral NTD proteins (Hulswit et al., 2019; Li et al., 2017; Ou et al., 2017; Peng et al., 2011). Taken together, we believe that the DcCoV UAE-HKU23 virus, with two conserved sugar-binding pockets in its spike NTD, shares the same sugar-recognition mechanism as BCoV, PHEV and HCoV-OC43. A more refined sugar-binding basis for HKU23-NTD, however, still awaits a complex structure of atomic resolution. Despite of intensified co-crystallization screenings, we have not been able to obtain the protein crystals of HKU23-NTD bound with any sugar molecules thus far.

2.4. A systematic comparison of the betaCoV NTD structures

Facilitated by the available betaCoV NTD structures, we were able to draw a clearer view on the evolution of the betaCoV NTD proteins via a detailed structural comparison. Despite of the limited sequence identities, these betaCoV NTDs share overall resembled structural folds, showing r.m.s.d. values ranging from 0.68 to 2.65 Å for the equivalent backbone Cα atoms (Table 2). The most conserved part is observed in the β-sandwich core (Fig. 4A–H). These sixteen anti-parallel β-strands, together with an inter-strand β8/β9 disulfide bond, are both structurally and topologically conserved. In addition, the peripheral element of the bottom α-helix is invariably reserved in all the NTD structures, which is anchored to the lower β-sheet layer by a conserved disulfide linkage.

In contrast to the β-sandwich core and the bottom helix that are individually of similar structures among different betaCoVs, the peripheral elements in the top-ceiling region and on the lateral side, however, show obvious structural variance. It is notable that with a conserved sandwich core, these ceiling and lateral components could be conceived as topological insertions between equivalent core-strands. In lineage A, six NTDs show a similar N-terminal component constituted by the β1′ strand. With the exception of HKU1-NTD, the other five lineage A NTDs contain the same β3/β4 insertion with two β-strands (β2′ and β3′) and one α-helix (α1). For the β8/β9 insertion, however, it is composed of a single loop in HKU1-NTD, but of a single β-strand (β4′) in MHV-NTD, and of two β-strands (β6′ and β7′) and one α-helix (α2) in HKU23-, BCoV-, PHEV- and HCoV-OC43-NTD. For the NTD β13/β14 insertion, DcCoV UAE-HKU23, BCoV, PHEV and HCoV-OC43 all contain a single β-strand (β8′), whereas HKU1 contains a single α-helix (α2). MHV, however, possesses both β-strand (β5′) and α-helix (α3). On the lateral side, instead of forming an inter-layer β-hairpin between β5 and β6 as observed in other five NTDs, MHV-NTD forms a lateral α-helix (α2) for this insertion (Fig. 4A–F). In lineage B, the core-strand insertions in SARS-NTD are predominated by four β-strands. These include two (β2′ and β3′) in the β8/β9 inter-linker, one (β1′) in the β3/β4 linker and one (β4′) in the β13/β14 linker, respectively. No lateral components, however, are observed in SARS-NTD (Fig. 4G). In lineage C, MERS-NTD is of the most complexity in terms of its strand-insertion composition, containing in total twelve β-strands and five α-helices (Fig. 4H). The N-terminal component comprises β1′ and α1. While both the β3/β4 and β13/β14 insertions are composed of two β-strands and one α-helix (β2′, β3′ and α2 for the β3/β4 insertion, and β11′, β12′and α5 for the β13/β14 insertion), the β8/β9 insertion includes three β-strands (β8′ - β10′) and two α-helices (α3 and α4). Finally on the lateral side, two β-hairpins (β4′/β5′ and β6′/β7′) are observed to be topologically inserted between core-strands β5/β6 and β6/β7, respectively, assembling as a “double-arm” to embrace the other insertions (Fig. 4H).

Despite of the variant structure-element compositions in the top-ceiling and the sandwich-lateral regions, one structurally and topologically conserved disulfide bond is observed in all the structures. It locates in the ceiling region, clinching the N-terminal element with the β8/β9 insertion to provide essential restraints for ceiling-element stabilization.

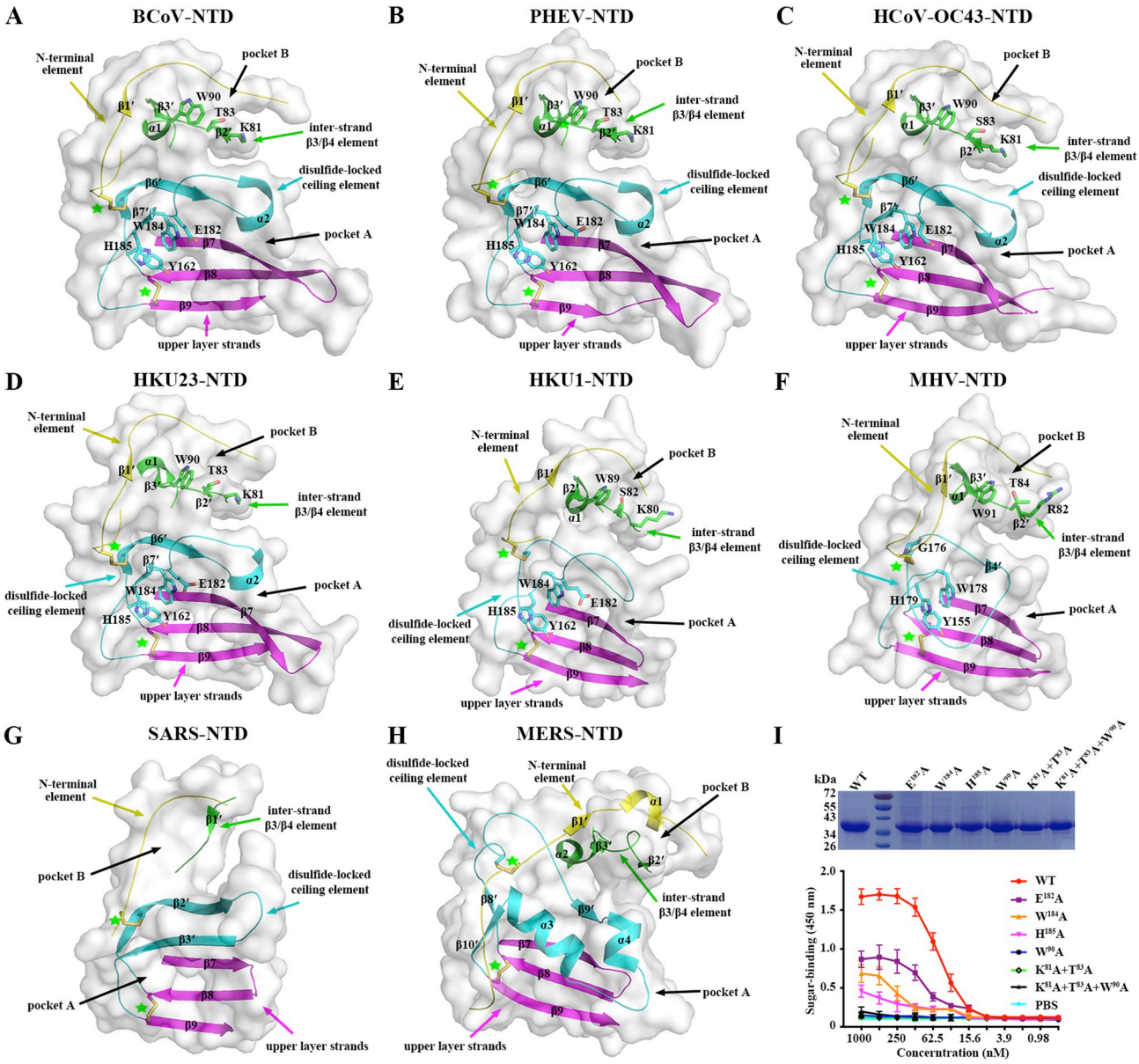

Fig. 3. Comparison of the two sugar-binding pockets in betaCoV NTDs. For pocket A, it is composed of a disulfide-locked ceiling element (cyan) and three upper-layer strands β7 - β9 (magenta). For pocket B, it comprises the inter-strand β3/β4 element (green) and an N-terminal element (orange). The tetra-residue motif (TRM) composed of Y162, E182, W184 and H185 in pocket A and the critical residues of K81, T83 and W90 within pocket B are highlighted and labeled. The disulfide bonds are displayed as sticks and indicated with green asterisks. (A) BCoV-NTD. (B) PHEV-NTD. (C) HCoV-OC43-NTD. (D) HKU23-NTD. (E) HKU1-NTD. (F) MHV-NTD. (G) SARS-NTD. (H) MERS-NTD. (I) A mutagenesis study characterizing the binding of indicated HKU23-NTD mutants to mucin. The upper panel shows the SDS-PAGE analyses of the mutant NTD proteins, and the lower panel presents the ELISA binding profiles.

Table 2
Statistics of the root mean square deviation (r.m.s.d) among available betaCoV NTD structures.

	HKU23-NTD	BCoV-NTD	HKU1-NTD	PHEV-NTD	HCoV-OC43-NTD	MHV-NTD	SARS-NTD	MERS-NTD
HKU23-NTD	–	0.72 Å (Cα 280)	1.28 Å (Cα 271)	0.88 Å (Cα 281)	0.71 Å (Cα 275)	1.22 Å (Cα 256)	2.34 Å (Cα 221)	2.29 Å (Cα 234)
BCoV-NTD		–	1.17 Å (Cα 273)	1.01 Å (Cα 285)	0.68 Å (Cα 282)	1.01 Å (Cα 256)	2.18 Å (Cα 220)	2.36 Å (Cα 237)
HKU1-NTD			–	1.23 Å (Cα 271)	1.22 Å (Cα 272)	1.19 Å (Cα 255)	2.20 Å (Cα 217)	2.65 Å (Cα 242)
PHEV-NTD				–	0.78 Å (Cα 274)	1.39 Å (Cα 259)	2.38 Å (Cα 225)	2.39 Å (Cα 234)
HCoV-OC43-NTD					–	1.07 Å (Cα 255)	2.33 Å (Cα 224)	2.40 Å (Cα 238)
MHV-NTD						–	2.21 Å (Cα 217)	2.55 Å (Cα 242)
SARS-NTD							–	2.54 Å (Cα 228)
MERS-NTD								–

The betaCoV NTD structures were superimposed onto each other by Coot in a pairwise manner to calculate the root mean square deviation (r.m.s.d) values, which were listed in the table. The values in parentheses indicate the number of equivalent Cα atoms that were selected for r.m.s.d calculations.

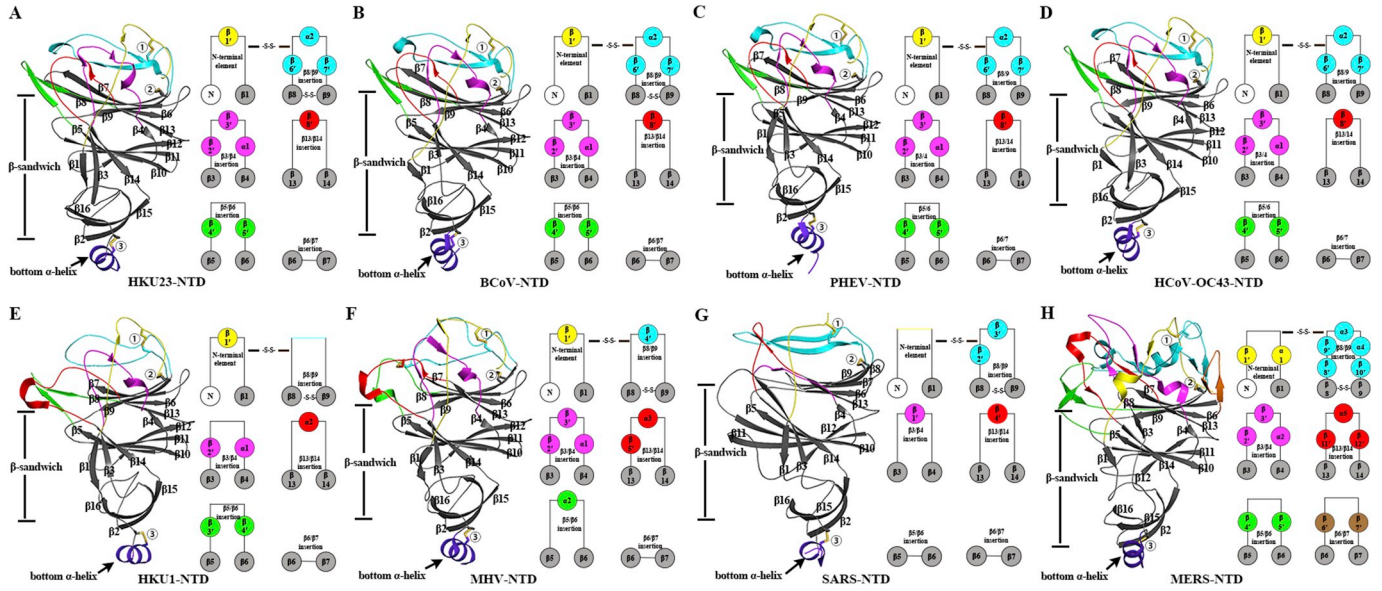

Fig. 4. A systematic comparison of the betaCoV NTD structures. The structures of eight betaCoV NTDs, including those from DcCoV UAE-HKU23 (reported in this study), BCoV (PDB code: 4H14), PHEV (PDB code: 6QFY), HCoV-OC43 (PDB code: 6OHW), HKU1 (PDB code: 5I08), MHV (PDB code: 3JCL), SARS-CoV (PDB code: 5X4S), and MERS-CoV (PDB code: 5X4R), are aligned in parallel in the same orientation and presented as cartoons. The β-sandwich core is colored gray. The bottom α-helix is colored purple. The N-terminal element is in yellow, and the inter-strand insertions are colored magenta for β3/β4 insertion, green for β5/β6 insertion, cyan for β8/β9 insertion, red for β13/β14 insertion and brown for β6/β7 insertion, respectively. Letter β marks the core-strands, and β′ and α individually mark the strands and helices in the peripheral elements. All the secondary structural elements are numbered according to their occurrence along the NTD amino acid sequence. The disulfide bonds are displayed as sticks and numbered. The right panel presents a schematic figure illustrating the composition of each core-strand insertions. (A) HKU23-NTD. (B) BCoV-NTD. (C) PHEV-NTD. (D) HCoV-OC43-NTD. (E) HKU1-NTD. (F) MHV-NTD. (G) SARS-NTD. (H) MERS-NTD.

3. Discussion

CoVs, especially betaCoVs, have imposed a severe threat to the global public health and have been described as the quintessential highly pathogenic human pathogens of the twenty-first century (Lu et al., 2015; Menachery et al., 2017). In the most cases of CoV infection, the CTD of the S1 subunit is prior over the NTD to function as the receptor-binding entity, whereas the NTD can sometimes facilitate CoV entry via binding to sugars, such as observed in the lineage A members of BCoV and HCoV-OC43 (Alejandra Tortorici et al., 2019; Hulswit et al., 2019; Peng et al., 2011, 2012). In this study, we demonstrated that DcCoV UAE-HKU23, which is a newfound member of lineage A betaCoV, can also recognize sugars via its S protein NTD. Furthermore, we also solved the crystal structure of HKU23-NTD and showed that it exhibits a resembled overall fold to other lineage A betaCoV NTDs. Guided by the previous studies characterizing the sugar-engagement sites in betaCoV NTDs (Hulswit et al., 2019; Peng et al., 2012), we successfully allocated two conserved sugar-binding pockets in the HKU23-NTD structure. Further mutagenesis study verified that both pockets play a role in the sugar recognition by the viral protein. With these experimental data, we believe DcCoV UAE-HKU23 utilizes the same mechanism to interact with sugars as other sugar-binding betaCoVs (e.g. BCoV and HCoV-OC43).

It should be noted that, within the NTD structures, pockets A and B are sterically close to each other (Fig. 3). Their steric adjacency might lead to allosteric interactions between the two pockets, explaining our observations that residue-substitutions in either pockets could affect the mucin-engagement by HKU23-NTD. It is also notable that amino acid mutations in pocket A only decreased the sugar interactions of HKU23-NTD, but residue mutations in pocket B could completely abolish the binding. Similar results have also been observed in HCoV-OC43-NTD (Hulswit et al., 2019). We therefore believe that pocket B likely plays a more dominant role than pocket A in sugar recognition. We also noticed that a recent study (Alejandra Tortorici et al., 2019) reported a cryo-EM structure of HCoV-OC43 spike in complex with 9-O-acetylated sialic acid (9-O-Ac-Sia), in which the 9-O-Ac-Sia moiety binds to pocket B in the spike NTD. In comparison to pocket B, pocket A is apparently of different residue-compositions and of larger size. This raises the possibility that pocket A has evolved to accommodate different sugar types (rather than 9-O-Ac-Sia) with relative lower-affinities than that observed between pocket B and 9-O-Ac-Sia.

It is also interesting that comparison of currently available betaCoV NTD structures reveals a conserved β-sandwich core. The top-ceiling and the lateral-side components, which are of variant compositions and folds, can thereby be dissected into element insertions between equivalent core-strands. In all the eight structures, the top-ceiling is composed of four insertions, including an N-terminal element and the β3/β4, β8/β9 and β13/β14 insertions. The number and composition of the lateral components, however, varies among different lineages. In lineage C, the MERS-NTD structure shows two lateral elements, one being inserted between strands β5 and β6 and the other one inserted between β6 and β7 (Fig. 5). In lineage A, all the six structures reveal a single lateral component, topologically forming the β5/β6 insertion. In comparison to that in lineage C, however, this β5/β6 insertion is of smaller size due to shortened amino acid sequence in the region (Fig. 5). In lineage B as observed with SARS-NTD, its structure is devoid of any lateral elements (Fig. 5). Finally in lineage D for which no NTD structure is available to date, the NTD sequence of bat coronavirus HKU9 clearly shows a single β5/β6 insertion as observed in lineage A. Nevertheless, this insertion is apparently of longer length (Fig. 5), drawing parallels between lineage C and lineage D viruses but differing HKU9 from members in lineage A. This is likely a unique feature for lineage D betaCoV NTDs. Taken together, we therefore believe that the lateral components of betaCoV NTD exhibit lineage-specific characteristics. While showing a conserved sandwich core of similar fold and of the same topological structure, the structural comparison also highlights that the betaCoV NTDs likely evolve from a common ancestor, which experiences divergent evolutions to form different lineages.

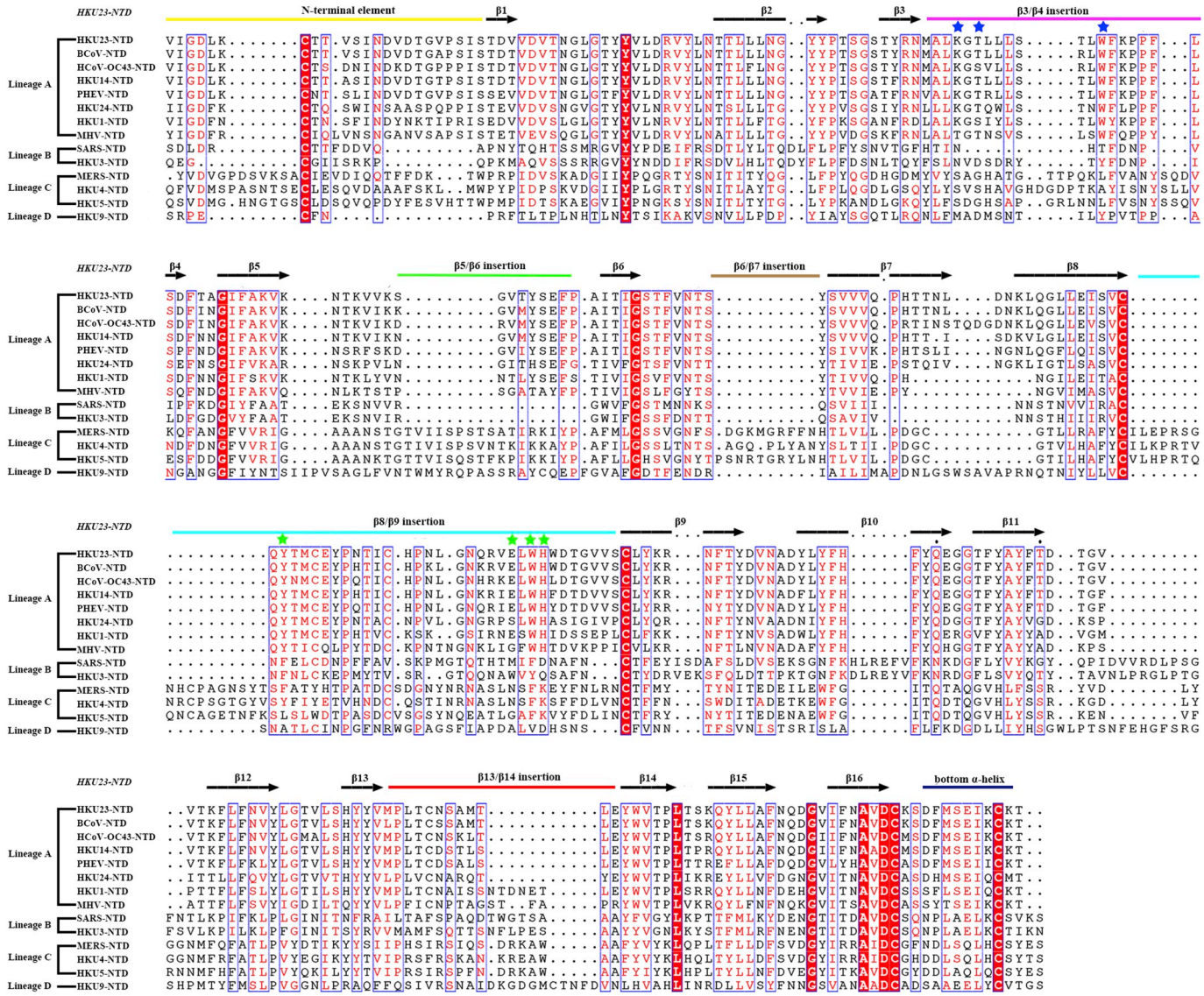

Fig. 5. Structure-based multiple sequence alignment of representative betaCoV NTDs. The strands of the β-sandwich core are labeled with black horizontal arrows. The peripheral structural elements, including the N-terminal element, five core-strand insertions and the bottom helix are indicated with horizontal lines colored the same way as in Fig. 4. The critical sugar-binding residues within pockets A and B are indicated with green and blue asterisks, respectively.

4. Materials and methods

4.1. Bioinformatic characterization of the HKU23 S sequence

The signal peptide (SP) extending from residues 1 to 14, transmembrane domain (TM) from residues 1311 to 1333 and two heptad repeat motifs (HR1 from 1015 to 1128 and HR2 from 1266 to 1299) of the DcCoV UAE-HKU23 spike protein were predicted with the SignalP 4.1 server, TMHMM server, and Learncoil-VMF program, respectively. The N- and C-terminal domains (NTD from 15 to 298 and CTD from 327 to 623), and fusion peptide (FP) from 916 to 927 were deduced by alignment with BCoV-NTD, SARS-CTD, and the FP of MERS-CoV spike, respectively.

4.2. Expression and purification of HKU23-NTD and its mutants

A synthetic insect codon-optimized sequence encoding the NTD (residues 15–298) of the spike protein from DcCoV UAE-HKU23 (GeneBank: AHN64783.1) was cloned into the pFastBac1 expression vector. A previously described GP67 signal peptide sequence (Han et al., 2017; Lu et al., 2013) was added to the protein N-terminus for protein secretion, and a 6 × His tag was added to the C-terminus to facilitate further purification processes. The protein was expressed and purified as described previously for other betaCoV NTDs (Peng et al., 2011, 2012; Yuan et al., 2017). Briefly, HKU23-NTD protein was prepared using the Bac-to-Bac baculovirus expression system (Invitrogen). The sequencing-verified recombinant pFastBac1 plasmid was transformed into DH10Bac competent cells to get the recombinant Bacmid, which was then transfected into Sf9 cells to get the primary baculovirus stock. Sf9 cells were then used to amplify the baculoviruses to obtain high-titer viral stocks, and High5 cells were used to express the protein. The supernatant of High5 culture was collected 72 h post-infection and passed through a 5 ml HisTrap HP column (GE Healthcare). The proteins bound to HisTrap were then detached by elution with gradient concentrations of imidazole. Subsequently, the target protein was further purified in an AKTA Pure System by gel filtration on a Superdex 200 increase 10/300 GL column (GE Healthcare) in the buffer consisting of 20 mM Tris-HCl (pH 8.0) and 150 mM NaCl. Finally, the eluted protein is pooled, analyzed for its purity by SDS-PAGE, and preserved for sugar-binding assays and crystallization.

The plasmids encoding the indicated HKU23-NTD mutants (including $E^{182}A$, $W^{184}A$, $H^{185}A$, $W^{90}A$, $K^{81}A+T^{83}A$ and $K^{81}A + T^{83}A+W^{90}A$), were generated by PCR-based site-directed mutagenesis. All the mutations were confirmed by DNA sequencing. The mutant proteins were prepared using the same procedures as described for the wild-type (WT) HKU23-NTD.

4.3. Sugar-binding assays

The capacity of His-tagged NTD proteins to bind to sugars was evaluated by ELISA using the bovine submaxillary gland mucin (BSM, Sigma-Aldrich). Briefly, 100 μl of mucin (60 μg/ml, diluted in PBS) was coated in the wells of 96-well Costar plates (Corning) by overnight incubation at 4 °C. Then the wells were dried completely, blocked with a 3% (w/v) bovine serum albumin (BSA) in PBS. Plates were then thoroughly washed with PBS containing 0.05% Tween-20, and subsequently incubated with twofold serial dilutions (starting at 1 μM) of His-tagged proteins (GST, WT and mutant HKU23-NTD) (prepared in this study), and SARS-NTD and MERS-NTD (a kind gift from Prof. George F. Gao's lab) at 4 °C for 2 h. The plates were then washed for five times with PBS, incubated with mouse anti-His antibody (Invitrogen) for 2 h, washed again for five times with PBS, incubated with horse radish peroxidase (HRP)-conjugated goat anti-mouse IgG antibody (1:5000), and washed, as a final washing stage, for five times again with PBS. Finally, the bound proteins were detected using Abbkine-ELISA-HRP substrates. The reaction wasstopped by addition of 1 N HCl. Optical density (OD) was subsequently measured at 450 nm with an ELISA reader.

4.4. Crystallization and data collection

The purified HKU23-NTD protein was concentrated to 10 mg/ml. The crystallization trials were performed with 1 μl protein mixing with 1 μl reservoir solution and then equilibrating against 70 μl reservoir solution by sitting drop vapor diffusion at 18 °C. The initial crystallization screening was performed using the commercially-available kits (Hampton Research and Molecular Dimensions). The conditions that support the growth of protein crystals were then optimized. High-quality crystals were finally obtained under a condition composed of 1.5 M Ammonium sulfate, and 0.1 M Sodium acetate trihydrate, pH 7.5. Diffraction data were collected at Shanghai Synchrotron Radiation Facility (SSRF) BL18U1. For data collection, all crystals were cryo-protected by briefly soaking in reservoir solution supplemented with 20% (v/v) glycerol before flash-cooling in liquid nitrogen. The collected data were processed using HKL2000 (Otwinowski and Minor, 1997) for indexing, integration, and scaling.

4.5. Structure determination

The structure of HKU23-NTD was determined by the molecular replacement method using Phaser (Fernandes et al., 2007) in the CCP4 suite (Winn et al., 2011) with the structure of BCoV-NTD (PDB: 4H14) as the search model. The atomic model was completed with Coot (Debreczeni and Emsley, 2012; Emsley and Cowtan, 2004). Rounds of refinement was performed with REFMAC5 (Murshudov et al., 2011), and finally with Phenix (Terwilliger et al., 2008; Zwart et al., 2008). The final model was assessed with PROCHECK (Laskowski et al., 1996). Final statistics for data collection and structure refinement are presented in Table 1. All structural figures were generated using PyMOL (http://www.pymol.org). The secondary structural elements are defined based on the Espript (Gouet et al., 1999). The HKU23-NTD structure has been deposited into the Protein Data Bank with a PDB code of 6JHY.

Conflicts of interest

The authors declare no conflict of interests.

Acknowledgments

This work was supported by the National Natural Science Foundation of China (Grant Nos. 31570157 and 81522026), the National Key R&D Program of China (Grant No. 2016YFC1200305), the Sichuan Outstanding Youth Science & Technology Funding (Grant No. 2016JQ0001), the Outstanding Youth Foundation of Sichuan University (Grant No. 2016SCU04B01). Dr. Yu Cao is supported in part by the National Natural Science Foundation of China (Grant Nos. 81772037 and 81471836), and the Chengdu Science and Technology Huimin Project (Grant No. 2016-HM02-00099-SF). We thank the staff of BL18U1 beamline at National Center for Protein Sciences Shanghai and Shanghai Synchrotron Radiation Facility (Shanghai, People's Republic of China) for assistance during data collection. The His-tagged MERS-NTD and SRAS-NTD proteins were a kind gift provided by Prof. George F. Gao at the Institute of Microbiology, Chinese Academy of Sciences.

References

Al-Tawfiq, J.A., Memish, Z.A., 2014. Middle East respiratory syndrome coronavirus: transmission and phylogenetic evolution. Trends Microbiol. 22, 573–579.

Alejandra Tortorici, M., Walls, A.C., Lang, Y., Wang, C., Li, Z., Koerhuis, D., Boons, G.J., Bosch, B.J., Rey, F.A., de Groot, R.J., Veesler, D., 2019. Structural basis for human coronavirus attachment to sialic acid receptors. Nat. Struct. Mol. Biol. 26 (6), 481–489. https://doi.org/10.1038/s41594-019-0233-y.

Bermingham, A., Chand, M.A., Brown, C.S., Aarons, E., Tong, C., Langrish, C., Hoschler, K., Brown, K., Galiano, M., Myers, R., Pebody, R.G., Green, H.K., Boddington, N.L., Gopal, R., Price, N., Newsholme, W., Drosten, C., Fouchier, R.A., Zambon, M., 2012. Severe respiratory illness caused by a novel coronavirus, in a patient transferred to the United Kingdom from the Middle East, September 2012. bulletin Europeen sur les maladies transmissibles = European communicable disease bulletin. Euro Surveill. 17, 20290.

de Groot, R.J., Baker, S.C., Baric, R.S., Brown, C.S., Drosten, C., Enjuanes, L., Fouchier, R.A., Galiano, M., Gorbalenya, A.E., Memish, Z.A., Perlman, S., Poon, L.L., Snijder, E.J., Stephens, G.M., Woo, P.C., Zaki, A.M., Zambon, M., Ziebuhr, J., 2013. Middle East respiratory syndrome coronavirus (MERS-CoV): announcement of the Coronavirus Study Group. J. Virol. 87, 7790–7792.

Debreczeni, J.E., Emsley, P., 2012. Handling ligands with Coot. Acta Crystallogr. Sect. D Biol. Crystallogr. 68, 425–430.

Desforges, M., Desjardins, J., Zhang, C., Talbot, P.J., 2013. The acetyl-esterase activity of the hemagglutinin-esterase protein of human coronavirus OC43 strongly enhances the production of infectious virus. J. Virol. 87, 3097–3107.

Emsley, P., Cowtan, K., 2004. Coot: model-building tools for molecular graphics. Acta Crystallogr. Sect. D Biol. Crystallogr. 60, 2126–2132.

Fernandes, P., Barois, P., Wang, S.T., Liu, Z.Q., McCoy, B.K., Huang, C.C., Pindak, R., Caliebe, W., Nguyen, H.T., 2007. Polarization studies of resonant forbidden reflections in liquid crystals. Phys. Rev. Lett. 99, 227801.

Forni, D., Cagliani, R., Clerici, M., Sironi, M., 2017. Molecular evolution of human coronavirus genomes. Trends Microbiol. 25, 35–48.

Gallagher, T.M., Buchmeier, M.J., 2001. Coronavirus spike proteins in viral entry and pathogenesis. Virology 279, 371–374.

Gouet, P., Courcelle, E., Stuart, D.I., Metoz, F., 1999. ESPript: analysis of multiple sequence alignments in PostScript. Bioinformatics 15, 305–308.

Han, X., Qi, J., Song, H., Wang, Q., Zhang, Y., Wu, Y., Lu, G., Yuen, K.Y., Shi, Y., Gao, G.F., 2017. Structure of the S1 subunit C-terminal domain from bat-derived coronavirus HKU5 spike protein. Virology 507, 101–109.

Hulswit, R.J.G., Lang, Y., Bakkers, M.J.G., Li, W., Li, Z., Schouten, A., Ophorst, B., van Kuppeveld, F.J.M., Boons, G.J., Bosch, B.J., Huizinga, E.G., de Groot, R.J., 2019. Human coronaviruses OC43 and HKU1 bind to 9-O-acetylated sialic acids via a conserved receptor-binding site in spike protein domain A. Proc. Natl. Acad. Sci. U.S.A. 116, 2681–2690.

Kirchdoerfer, R.N., Cottrell, C.A., Wang, N., Pallesen, J., Yassine, H.M., Turner, H.L., Corbett, K.S., Graham, B.S., McLellan, J.S., Ward, A.B., 2016. Pre-fusion structure of a human coronavirus spike protein. Nature 531, 118–121.

Kunkel, F., Herrler, G., 1993. Structural and functional analysis of the surface protein of human coronavirus OC43. Virology 195, 195–202.

Lai, M.M.C., Perlman, S., Anderson, L.J., 2007. Coronaviridae. In: Fields Virology, pp. 1305–1336.

Laskowski, R.A., Rullmannn, J.A., MacArthur, M.W., Kaptein, R., Thornton, J.M., 1996. AQUA and PROCHECK-NMR: programs for checking the quality of protein structures solved by NMR. J. Biomol. NMR 8, 477–486.

Li, W., Hulswit, R.J.G., Widjaja, I., Raj, V.S., McBride, R., Peng, W., Widagdo, W., Tortorici, M.A., van Dieren, B., Lang, Y., van Lent, J.W.M., Paulson, J.C., de Haan, C.A.M., de Groot, R.J., van Kuppeveld, F.J.M., Haagmans, B.L., Bosch, B.J., 2017. Identification of sialic acid-binding function for the Middle East respiratory syndrome

coronavirus spike glycoprotein. Proc. Natl. Acad. Sci. U.S.A. 114, E8508–e8517.
Li, W., Moore, M.J., Vasilieva, N., Sui, J., Wong, S.K., Berne, M.A., Somasundaran, M., Sullivan, J.L., Luzuriaga, K., Greenough, T.C., Choe, H., Farzan, M., 2003. Angiotensin-converting enzyme 2 is a functional receptor for the SARS coronavirus. Nature 426, 450–454.
Li, W., Sui, J., Huang, I.C., Kuhn, J.H., Radoshitzky, S.R., Marasco, W.A., Choe, H., Farzan, M., 2007. The S proteins of human coronavirus NL63 and severe acute respiratory syndrome coronavirus bind overlapping regions of ACE2. Virology 367, 367–374.
Lu, G., Hu, Y., Wang, Q., Qi, J., Gao, F., Li, Y., Zhang, Y., Zhang, W., Yuan, Y., Bao, J., Zhang, B., Shi, Y., Yan, J., Gao, G.F., 2013. Molecular basis of binding between novel human coronavirus MERS-CoV and its receptor CD26. Nature 500, 227–231.
Lu, G., Wang, Q., Gao, G.F., 2015. Bat-to-human: spike features determining 'host jump' of coronaviruses SARS-CoV, MERS-CoV, and beyond. Trends Microbiol. 23, 468–478.
Menachery, V.D., Graham, R.L., Baric, R.S., 2017. Jumping species-a mechanism for coronavirus persistence and survival. Curr. Opin. Virol. 23, 1–7.
Murshudov, G.N., Skubak, P., Lebedev, A.A., Pannu, N.S., Steiner, R.A., Nicholls, R.A., Winn, M.D., Long, F., Vagin, A.A., 2011. REFMAC5 for the refinement of macromolecular crystal structures. Acta Crystallogr. Sect. D Biol. Crystallogr. 67, 355–367.
Otwinowski, Z., Minor, W., 1997. [20] Processing of X-ray diffraction data collected in oscillation mode. Methods Enzymol. 276, 307–326.
Ou, X., Guan, H., Qin, B., Mu, Z., Wojdyla, J.A., Wang, M., Dominguez, S.R., Qian, Z., Cui, S., 2017. Crystal structure of the receptor binding domain of the spike glycoprotein of human betacoronavirus HKU1. Nat. Commun. 8, 15216.
Peng, G., Sun, D., Rajashankar, K.R., Qian, Z., Holmes, K.V., Li, F., 2011. Crystal structure of mouse coronavirus receptor-binding domain complexed with its murine receptor. Proc. Natl. Acad. Sci. U.S.A. 108, 10696–10701.
Peng, G., Xu, L., Lin, Y.L., Chen, L., Pasquarella, J.R., Holmes, K.V., Li, F., 2012. Crystal structure of bovine coronavirus spike protein lectin domain. J. Biol. Chem. 287, 41931–41938.
Ravindranath, M.H., Higa, H.H., Cooper, E.L., Paulson, J.C., 1985. Purification and characterization of an O-acetylsialic acid-specific lectin from a marine crab Cancer antennarius. J. Biol. Chem. 260, 8850–8856.
Schultze, B., Gross, H.J., Brossmer, R., Herrler, G., 1991. The S protein of bovine coronavirus is a hemagglutinin recognizing 9-O-acetylated sialic acid as a receptor determinant. J. Virol. 65, 6232–6237.
Su, S., Wong, G., Shi, W., Liu, J., Lai, A.C.K., Zhou, J., Liu, W., Bi, Y., Gao, G.F., 2016. Epidemiology, genetic recombination, and pathogenesis of coronaviruses. Trends Microbiol. 24, 490–502.
Terwilliger, T.C., Grosse-Kunstleve, R.W., Afonine, P.V., Moriarty, N.W., Zwart, P.H., Hung, L.W., Read, R.J., Adams, P.D., 2008. Iterative model building, structure refinement and density modification with the PHENIX AutoBuild wizard. Acta Crystallogr. Sect. D Biol. Crystallogr. 64, 61–69.
Vabret, A., Mourez, T., Gouarin, S., Petitjean, J., Freymuth, F., 2003. An outbreak of coronavirus OC43 respiratory infection in Normandy, France. Clin. Infect. Dis. 36, 985–989.
Wang, Q., Qi, J., Yuan, Y., Xuan, Y., Han, P., Wan, Y., Ji, W., Li, Y., Wu, Y., Wang, J., Iwamoto, A., Woo, P.C., Yuen, K.Y., Yan, J., Lu, G., Gao, G.F., 2014a. Bat origins of MERS-CoV supported by bat coronavirus HKU4 usage of human receptor CD26. Cell Host Microbe 16, 328–337.
Wang, S.M., Huang, K.J., Wang, C.T., 2014b. BST2/CD317 counteracts human coronavirus 229E productive infection by tethering virions at the cell surface. Virology 449, 287–296.
Weinstein, R.A., 2004. Planning for epidemics–the lessons of SARS. N. Engl. J. Med. 350, 2332–2334.
WHO, 2019. MERS Situation Update, January 2019.
Winn, M.D., Ballard, C.C., Cowtan, K.D., Dodson, E.J., Emsley, P., Evans, P.R., Keegan, R.M., Krissinel, E.B., Leslie, A.G., McCoy, A., McNicholas, S.J., Murshudov, G.N., Pannu, N.S., Potterton, E.A., Powell, H.R., Read, R.J., Vagin, A., Wilson, K.S., 2011. Overview of the CCP4 suite and current developments. Acta Crystallogr. Sect. D Biol. Crystallogr. 67, 235–242.
Woo, P.C., Lau, S.K., Chu, C.M., Chan, K.H., Tsoi, H.W., Huang, Y., Wong, B.H., Poon, R.W., Cai, J.J., Luk, W.K., Poon, L.L., Wong, S.S., Guan, Y., Peiris, J.S., Yuen, K.Y., 2005. Characterization and complete genome sequence of a novel coronavirus, coronavirus HKU1, from patients with pneumonia. J. Virol. 79, 884–895.
Woo, P.C., Lau, S.K., Fan, R.Y., Lau, C.C., Wong, E.Y., Joseph, S., Tsang, A.K., Wernery, R., Yip, C.C., Tsang, C.C., Wernery, U., Yuen, K.Y., 2016. Isolation and characterization of dromedary camel coronavirus UAE-HKU23 from dromedaries of the Middle East: minimal serological cross-reactivity between MERS coronavirus and dromedary camel coronavirus UAE-HKU23. Int. J. Mol. Sci. 17.
Woo, P.C., Lau, S.K., Wernery, U., Wong, E.Y., Tsang, A.K., Johnson, B., Yip, C.C., Lau, C.C., Sivakumar, S., Cai, J.P., Fan, R.Y., Chan, K.H., Mareena, R., Yuen, K.Y., 2014. Novel betacoronavirus in dromedaries of the Middle East, 2013. Emerg. Infect. Dis. 20, 560–572.
Yuan, Y., Cao, D., Zhang, Y., Ma, J., Qi, J., Wang, Q., Lu, G., Wu, Y., Yan, J., Shi, Y., Zhang, X., Gao, G.F., 2017. Cryo-EM structures of MERS-CoV and SARS-CoV spike glycoproteins reveal the dynamic receptor binding domains. Nat. Commun. 8, 15092.
Zeng, Q., Langereis, M.A., van Vliet, A.L., Huizinga, E.G., de Groot, R.J., 2008. Structure of coronavirus hemagglutinin-esterase offers insight into corona and influenza virus evolution. Proc. Natl. Acad. Sci. U.S.A. 105, 9065–9069.
Zwart, P.H., Afonine, P.V., Grosse-Kunstleve, R.W., Hung, L.W., Ioerger, T.R., McCoy, A.J., McKee, E., Moriarty, N.W., Read, R.J., Sacchettini, J.C., Sauter, N.K., Storoni, L.C., Terwilliger, T.C., Adams, P.D., 2008. Automated structure solution with the PHENIX suite. Methods Mol. Biol. 426, 419–435.